Environmental Science Nano

ROYAL SOCIETY OF CHEMISTRY

PAPER

View Article Online
View Journal | View Issue

Cite this: *Environ. Sci.: Nano*, 2025, **12**, 1979

Facet-dependent growth and dissolution of hematite resulting from autocatalytic interactions with Fe(II) and oxalic acid†

Sandra D. Taylor, *[a] John B. Cliff, ‡[b] Thomas W. Wietsma [b] and Kevin M. Rosso *[a]

The ability to simultaneously monitor the flux of iron atoms within the solution and solid phases can provide considerable insight into mechanisms of iron oxide mineral transformations. The autocatalytic interaction between hematite and Fe(II)-oxalate has long been of interest for its environmental and industrial relevance. In this study we take advantage of iron isotopic labelling and mass-sensitive imaging at the single particle scale to determine how changes in solution composition correlate with the morphologic evolution of faceted, micrometer-sized hematite platelets. Net dissolution is confirmed through analyses of aqueous iron chemistry, as well as by quantitative atomic force microscopy. Isotopic mapping techniques show that Fe(II) readily adsorbs to (001) and (012) surfaces in the absence of oxalate, but when oxalate is present selective dissolution of the (001) surface prevails and Fe deposition *via* recrystallization is not observed. Comparison between particle microtopographies following reaction with Fe(II), oxalate, and Fe(II)-oxalate show substantially different behaviors, consistent with distinct mechanisms of interaction with hematite surfaces. The extensive characterization conducted on the coupled solution/solid dynamics in this system provides new insight for distinguishing crystal growth, dissolution, and recrystallization processes.

Received 25th October 2024,
Accepted 21st January 2025

DOI: 10.1039/d4en01004c

rsc.li/es-nano

Environmental significance

Growth, dissolution, and recrystallization of Fe-(oxyhydr)oxides controls the biogeochemical cycling of iron as well as other metals, nutrients, and contaminants. Interactions with redox-active metal solutes and/or natural chelates play an important role. For instance, reductive dissolution as well as recrystallization of hematite can occur through synergistic interactions between Fe(II) and natural carboxylic acids at the mineral–water interface. An important unknown is the combined effect of these components on the mass transport pathways of iron. By combining spectrometric, microscopic, and isotopic tracer techniques with morphologically precise hematite microplatelets, our study highlights how specific interfacial structures determine the propensity for growth, dissolution, and recrystallization behavior. The findings will help inform a new generation of predictive models based on the molecular details at structurally specific mineral–water interfaces.

Introduction

The growth, dissolution, and recrystallization of Fe-(oxyhydr) oxides are processes central to the biogeochemical cycling of Fe, as well as other metals, nutrients, and contaminants that couple to iron speciation in the environment. At redox transition zones, the interaction of $Fe(II)_{aq}$ with Fe-(oxyhydr) oxides is of particular importance for its autocatalytic potential, enabled by the prospect of Fe(II)–Fe(III) intervalence charge transfer.[1] More so, $Fe(II)_{aq}$ complexation with carboxylate-rich organic compounds in nature, such as oxalic acid ($C_2H_2O_4$) exuded by plants and microorganisms, also influences transformations of nominally stable Fe(III)-oxides such as goethite (α-FeOOH) and hematite (α-Fe_2O_3).[2,3] That is, early experimental studies reacting iron oxide minerals with Fe(II) and oxalic acid in solution observed accelerated mineral dissolution rates, particularly at low pH,[3,4] suggesting formation of a stronger reducing complex than the bare iron or oxalate aquo ions. While sensitive to a number of variables (*e.g.*, pH, temperature, reductant and/or chelating ligand concentrations, *etc.*), synergistic interactions between oxalic acid and ferrous ions in solution are speculated to follow fundamental molecular-level steps: (i) the formation of Fe(II)-oxalato complexes in solution; (ii)

[a] *Physical and Computational Sciences Directorate, Physical Sciences Division, Pacific Northwest National Laboratory, Richland, WA 99352, USA. E-mail: sandra.taylor@pnnl.gov, kevin.rosso@pnnl.gov*
[b] *Earth and Biological Sciences Directorate, Pacific Northwest National Laboratory, Richland, WA 99352, USA*

† Electronic supplementary information (ESI) available: ESI is available in a separate file. See DOI: https://doi.org/10.1039/d4en01004c

‡ New address: National Security Directorate, Oak Ridge National Laboratory, Oak Ridge, TN 37830, USA.

adsorption and formation of ternary complexes onto iron oxide surfaces, with oxalate bridging $Fe(II)_{aq}$ to $Fe(III)_{(s)}$; and (iii) electron transfer across the bridging Fe(II)–Fe(III) complex, facilitating surface Fe(III) reduction and release into solution.[3,5–8] Fe(II) in solution is also effectively recycled during reaction, in turn propagating autocatalytic reaction.

Studies exploring these synergistics effects and enhanced reactivity at the mineral-water interface point to the critical role of the Fe(II)–Fe(III) electron exchange step. Understanding the interfacial reactivity of hematite may also be further complicated by electron electron exchange processes potentially being coupled across common surfaces (*i.e.*, the basal (001) surface as well as (012) and (110) edge surfaces) by solid-state electron conduction, as put forth by Yanina and Rosso.[9] Evidence was obtained through experiments directly monitoring the surface potentiometry and evolving microtopography over hematite bicrystals during reaction with $Fe(II)_{aq}$ and oxalic acid; specific surface exposures on the bicrystals were controlled using oriented macroscopic crystals exposing (001) and saw-cut (*hk*0) edge surfaces, connected by a conductive (Ag) paste. Distinct morphologic evolution was observed depending on the configuration. That is, when (001) and edge surfaces were both exposed and electrically connected, edge surfaces showed features characteristic of dissolution, such as fine-scale pitting and roughening, whereas the (001) surface became extensively covered in hexagonal pseudo-pyramids. Similar morphologic evolution was also observed using synthetic tabular hematite single crystals bearing primarily (001) and (012) surfaces.[10] In contrast, the morphologic evolution of bicrystals was distinctly different when (001) and edge surfaces were not electrically connected (*i.e.*, pyramidal surface features did not form), thus asserting the role of solid-state conduction. Mass transfer of iron from one surface (*e.g.*, edge surfaces) to another (*e.g.*, (001)) was determined largely on the basis of the measured sign of the surface electrostatic potential gradient between them. It is noteworthy that across all these bespoke studies, from powders to single crystals, there are differences in potentially crucial system variables, including the reaction temperature, pH, relative concentrations of $Fe(II)_{aq}$ and oxalate, the solid-to-solution mass loading impacting the amount of reactive surface area, the physical properties of the hematite (*e.g.*, conductivities of natural *versus* synthetic crystallites,[11,12] presence of impurities, relative surface expression, particle aspect ratios, *etc.*), as well as consequential differences in the ability to monitor important system quantities such as the Fe(II) and Fe(III) concentrations in solution over time.

Such observations nonetheless raise important questions about the mass transport processes during autocatalytic reaction of Fe(II) with iron oxides such as hematite enhanced by the presence of chelating ligands. This is particularly true for conditions poised for recrystallization where both dissolution and growth may be occurring simultaneously between specific facets/sites. Reactivities of distinct surfaces being either interdependent or independent of each other has broad implications for understanding chemical behaviors at mineral-water interfaces, from impacting mineral transformations during soil evolution to engineering facet-specific materials for the remediation of environmental pollutants.[13–16] However, this understanding remains limited due to the experimental challenges in monitoring the flux of elementally identical atoms from the solution to the solid phase as well as between solid interfaces.[1,17] Recent advances utilizing stable isotopic-labelling of reacting Fe pools combined with high-resolution mass-sensitive characterization techniques, *i.e.*, nanoscale secondary ion mass spectrometry (NanoSIMS) and three-dimensional atom probe tomography (3D APT), can provide direct insight into autocatalytic mass transport processes at mineral-water interfaces; for instance previous studies demonstrate oxidative adsorption of $Fe(II)_{aq}$ occurs preferentially on the hematite (001) surface at neutral pH.[18–20]

In this study, we probed competitive growth and/or dissolution processes within the the Fe(II)-oxalate-hematite system, to understand how structural details at surfaces govern the labilization and transport of iron. The selected experimental conditions approximate but do not duplicate those in the aqueous ^{57}Fe(II)-oxalate-hematite microplatelet studies of Rosso, *et al.*,[10] Separate interactions of Fe(II) and oxalate with hematite were also examined. The flux of iron atoms between solid and solution phases as well as between solid surfaces was followed, utilizing ^{57}Fe-labelled ferrous iron in solution coupled with multimodal analytical techniques. That is, soluble Fe(II) and Fe(III) concentrations as well as the aqueous iron isotopic concentrations were measured by ultraviolet-visible spectroscopy (UV-vis) and inductively-coupled plasma mass spectrometry (ICP-MS), respectively, to determine whether net dissolution or growth occurs over the different reaction conditions. NanoSIMS and 3D APT were used to follow the redistribution of ^{57}Fe, introduced in the initial $Fe(II)_{aq}$ fraction, across hematite surfaces. The microtopographic evolution across hematite surfaces was also observed *ex situ* by scanning electron microscopy (SEM). Further, quantitative analyses of surface-specific dissolution *vs.* growth was achieved by measuring morphological changes in identical particles by *ex situ* atomic force microscopy (AFM).

In brief, we find that $Fe(II)_{aq}$ alone can adsorb to (001) and (012) surfaces yielding net growth, whereas in the presence of oxalate, net dissolution is observed to selectively occur on (001). More so, the multimodal analyses conclusively demonstrate highly anisotropic and facet-dependent dissolution resulting from synergistic interactions between $Fe(II)_{aq}$ and oxalate compared to oxalate alone, including the appearance of the pyramidal microtopography on (001). The findings reinforce the current picture of synergistic reductive dissolution effects in the Fe(II)-oxalate-hematite system, with morphologic outcomes that are sensitive to the microscopic details defining local conditions at particle surfaces. These new observations expand our insights into dissolution-readsorption processes of broad significance to understanding mineral recrystallization.

Methods

Batch experiments were conducted reacting hematite microplatelets at natural isotopic abundance (NA) in pH 2.3 solutions with oxalic acid, ^{57}Fe(II), and ^{57}Fe(II)-oxalic acid at 75 °C for 24 h using Parr acid digestion vessel setup. These reactions were selected to systematically examine different dissolution reactions and mechanisms (*e.g.*, proton-, reductive-, ligand-, and reductive/ligand-promoted dissolution, respectively). We emphasize that the initial Fe(II) solutions were enriched in ^{57}Fe (96%) to enable monitoring iron atom exchange between solution and solid phases. Control experiments (*e.g.*, with non-labelled Fe(II)) were also conducted. Two different sets of experiments were conducted in this study where, in brief, the first set aimed to reproduce observations most similar to ^{57}Fe(II)-oxalate-hematite experiments in Rosso, *et al.*,[10] to gain further insight as to whether recrystallization and atom exchange occur using mass-sensitive imaging techniques. The second set of experiments were designed to directly observe and measure changes in particle microtopography by AFM *ex situ*, capturing facet- and/or site-specific dissolution/growth processes under the various reaction conditions. The experimental setup and reaction conditions are described in detail below in the "Bulk batch experiments" and "AFM-centric batch experiments" sections, respectively. As mentioned above, various techniques were utilized to follow the flux of iron atoms between the solids and solution phases as well as at solid surfaces, including UV-vis, ICP-MS, SEM, NanoSIMS, and 3D APT. Details for the different analytical protocols are provided in the (ESI†).

Materials preparation

Micrometer-sized hematite platelets with isotopic concentrations at NA were synthesized according to Sapieszko and Matijevic.[21] As characterized in previous studies,[18] the particles exhibit well-defined (001) basal and (012) edge surfaces. The basal surface is dominant, where the microscale topography often exhibits bunched step waves emanating from central growth spirals, providing evidence for dislocations near the centers of platelets. The (012) edge surfaces appear smooth and regular.[22] Many particles also exhibit defects at their surfaces such as intergrowth pits, which are sites where single crystals appear to attach and coalesce. These defects are typically nano-faceted expressing various edge facets such (012), (110) and (014). The specific surface area of the particles was measured to be 0.2 $m^2\ g^{-1}$ using the Brunauer–Emmett–Teller method with N_2 adsorption and a degas temperature of 100 °C.

Reactions were conducted by diluting stock solutions of 0.1 M KCl, 0.1 M oxalic acid, and 0.08 M ^{57}Fe(II); further preparation details are provided in the ESI,† section 1. The respective solutions were prepared from anoxic, degassed water. ^{57}Fe-labelled metal (96%, Cambridge Isotopes) was dissolved in 0.3 M HCl, according to the procedure described by Taylor, *et al.*[19] Control experiments were also conducted, using a stock solution of 0.1 M Fe(II) at NA.

Bulk batch experiments

For the first set of batch experiments, ~10 mg of the hematite powder was reacted with 12.5 mL, pH 2.3 solutions of (i) 10 mM KCl, (ii) 1 mM ^{57}Fe(II) + 10 mM KCl, (iii) 10 mM oxalic acid + 10 mM KCl, and (iv) 1 mM ^{57}Fe(II) + 10 mM oxalic acid + 10 mM KCl, in 23 mL Parr digestion vessels at 75 °C for 24 h. A control experiment for the reductive/ligand-promoted reaction was also conducted, where the hematite particles were reacted with oxalic acid and Fe(II) at NA. We refer to these different reactions as "KCl-hematite," "^{57}Fe(II)-hematite," "oxalate-hematite," "^{57}Fe(II)-oxalate-hematite," and "^{NA}Fe(II)-oxalate-hematite" throughout the text.

The ^{57}Fe(II)-oxalate-hematite experiments here are similar to those conducted in Rosso, *et al.*,[10] including ^{57}Fe-enrichment of the initial Fe(II) solution and utilizing micrometer-sized hematite microplatelets reproducing the relative surface expressions. However, the previous study was done using a lower mass loading of particles (*i.e.*, ~10 mg of the hematite microplatelets were reacted in 125 mL of 1 mM ^{57}Fe(II)-10 mM oxalic acid solution at pH 2.1 for 24 h in a 125 mL Parr digestion vessels at 75 °C). Here, a 10× higher mass loading enabled easier recovery of reacted solids for characterization, *i.e.*, at lower loadings hematite could not readily be retrieved due to more prolific dissolution or adsorption to the Teflon walls of the Parr vessel. The hematite surfaces should nonetheless be saturated relative to Fe(II) and oxalate for the experiments in this study and Rosso, *et al.*;[10] *i.e.*, assuming surface coverage is 2.5 sites nm^{-2} (a value consistent with the average lattice Fe site density) and adsorption of both Fe(II) and oxalate occurs as mononuclear complexes,[8] monolayer coverage for these particles is estimated to be ~0.8 μmol g^{-1}.[19] Further, while the system conditions are categorically different than previous studies, qualitatively similar evolution in surface microtopographic features were still observed (discussed below).

Details of the batch experimental procedures are described in the ESI,† section 2.1. In brief, experiments were conducted in an anoxic glovebox (93% N_2/7% H_2 atmosphere). Care was taken to avoid exposing the reactions and solutions to light, to prevent potential photoreduction reactions by oxalate,[23] by working away from light and using amber tubes during solution preparation. For each reaction, ~10 mg of the hematite microplatelets were placed into separate 23 mL Teflon cups inserts of the Parr digestion vessels. The respective solutions were added to the vessels, which were closed, sealed, and reacted at ~75 °C in a rotary oven (~50 rpm) outside of the glovebox for 24 h. After reaction, the reactors were cooled in an ice bath for ~2–3 minutes and transferred back into the glovebox for sampling of the aqueous and solid fractions.

The supernatant was removed *via* centrifugation and filtered through a 0.22 μm membrane to remove particulates

(again avoiding exposure to light) and reserved for aqueous analysis. Aqueous analytical protocols are described in the ESI,† section 2.1. In brief, total iron (Fe_{tot}) as well as Fe(II) and Fe(III) concentrations in solution ($Fe(II)_{aq}$ and $Fe(III)_{aq}$, respectively) before and after reaction were measured by UV-vis by the ferrozine method.[24] Iron isotopic concentrations in solution were determined by ICP-MS. The most dominant isotopes in this study, *i.e.*, ^{57}Fe and ^{56}Fe, were more specifically analyzed to follow the extent of iron atom exchange and/or mixing during contact between the ^{57}Fe-spiked solution *vs.* hematite naturally dominant in ^{56}Fe (91.8%). The concentration for ^{57}Fe is in turn expressed as a fraction ($f_{^{57}Fe}$) relative to ^{56}Fe (eqn (1)):

$$f_{^{57}Fe} = \frac{n_{57}}{n_{56} + n_{57}} \quad (1)$$

where n is the counts per second of ^{57}Fe and ^{56}Fe isotopes.

For characterization of the solid phase, weakly bound Fe(II) on the hematite was removed by rinsing the particles with water and exposing them to 0.4 M HCl for 10 minutes, thus allowing focus on the more strongly interacting Fe(II) fraction such as that attributable to the process of oxidative adsorption consistent with surface recrystallization.[18,19] Following the acid extraction step, the particles were rinsed two more times with the anoxic Milli-Q water and dried overnight in the anoxic glovebox. SEM was used to observe general changes in morphology for the various reactions. Isotopic distributions and measurements within the $^{57}Fe(II)$-oxalate-hematite system were also obtained using high mass-resolving techniques, *i.e.*, NanoSIMS and 3D APT, where spatial and temporal analyses at the micrometer and nanometer-scale can provide insight into potential recrystallization phenomena. The $^{57}Fe(II)$-hematite and $^{NA}Fe(II)$-oxalate-hematite systems were analyzed by NanoSIMS as control samples. NanoSIMS and APT analyses were done similar to previous studies,[18,19] with modifications to instrumental parameters as needed (see ESI† sections 2.3 and 2.4, respectively, for details of analytical procedures).

AFM-centric batch experiments

For the second set of experiments, ~0.5 mg of hematite was first dispersed onto high purity vitreous carbon planchets (10 mm diameter) which were then reacted in 12.5 mL, pH 2.3 solutions of (i) 0.50 mM KCl, (ii) 0.050 mM $^{57}Fe(II)$ + 0.50 mM KCl, (iii) 0.50 mM oxalic acid + 0.50 mM KCl, and (iv) 0.05 mM $^{57}Fe(II)$ + 0.50 mM oxalic acid + 0.50 mM KCl. We refer to these reactions like that mentioned above but denote them with an asterisk; *e.g.*, the $^{57}Fe(II)$ and oxalic acid exposure here is referred to as "$^{57}Fe(II)$-oxalate-hematite*." Particles affixed onto the planchets enabled microtopographic analyses by AFM in contact mode. Further, the substrates provided sufficiently smooth reference surfaces (*e.g.*, ~10–20 nm RMS roughness), enabling net dissolution *vs.* growth along the [001] direction of the tabular platelets to be distinguished based on changes in the thicknesses of identical particle relative to the underlying substrate before and after reaction. AFM measurements were collected over several particles on each planchet before reaction, capturing the as-grown microtopography (see ESI† section 2.2 for details on the AFM analytical protocol). Particle locations were identifiable relative to fiducial markers on the substrate (*e.g.*, roman numerals scratched into the substrate), therefore enabling analyses of the same particles after reaction, following the same protocol used for the before-reaction imaging. Here, for each reaction, the microtopography of one particle is highlighted as a representative specimen. The aqueous iron concentration and isotopic composition was also measured by UV-vis and ICP-MS.

A lower mass loading compared to the bulk batch experiments was used here (*i.e.*, 0.05× lower), as it allowed single particles to be isolated and imaged with AFM; higher loadings would introduce aggregates incompatible with AFM imaging. In turn, the solution concentrations were similarly scaled down by 0.05×. The mass loadings are also slightly lower than that used in Rosso, *et al.*[10] (*i.e.*, 0.5×), resulting in similar considerations about attendant differences in conditions. However, when combined with the loose powder experiments, the collective conditions deployed conceptually "bracket" those previously used.[10]

The above-mentioned Parr acid digestion vessel setup for the bulk batch experiments was used here with a few modifications. For instance, to minimize particles from being dislodged from the planchet during mixing in the oven, the planchet was adhered to the bottom of the 23 mL Teflon cup using double-sided tape. The additional variables introduced (*e.g.*, the planchet, double-sided tape, *etc.*,) were not found to affect measurements as the particle microtopography for the standard KCl-hematite* specimen could be reproduced within error (discussed below). Additionally, minimal cleaning was done to prevent particles from being dislodged from the planchet to enable post-reaction AFM imaging of the same particles measured pre-reaction.

Results

Assessing net growth *vs.* dissolution of hematite by aqueous iron analyses

The iron concentration, valence, and isotopic composition in the solution from the bulk batch experiments were characterized using UV-vis and ICP-MS (Table 1), respectively, to gain insight into mass transport across the solid/solution interface as well as the evolution of the iron isotopic composition of the solution. Changes in iron concentrations following reaction (*i.e.*, ΔFe_{tot}, $\Delta Fe(II)_{aq}$ and $\Delta Fe(III)_{aq}$) provide insight into whether net dissolution or growth by adsorption occurs following reaction as reflected by aqueous iron concentrations in excess or below that initially present in solution, respectively. Additionally, the iron valence state in solution provides insight into the dissolution mechanism (*e.g.*, reductive *vs.* ligand-controlled) while the iron isotopic

Table 1 Changes in soluble iron concentrations and isotopic composition across the different reactions in the bulk batch and AFM-centric experiments

	Initial reagent concentrations[a]				Aqueous iron concentrations[b] (mM)			$f_{^{57}Fe}$[c]	
Bulk batch experiments	Hematite (g L^{-1})	KCl (mM)	Fe(II) (mM)	Oxalic acid (mM)	ΔFe_{tot}	$\Delta Fe(II)_{aq}$	$\Delta Fe(III)_{aq}$	Before	After
^{57}Fe(II), aqueous control	—	10.0	1.00	—	−0.03	−0.03	0.00	0.95	0.94
KCl-hematite	0.80	10.0	—	—	0.00	0.00	0.00	—	—
^{57}Fe(II)-hematite	0.80	10.0	1.00	—	−0.07	−0.07	0.00	0.95	0.98
Oxalate-hematite	0.80	10.0	—	10.0	1.17	0.44	0.73	—	0.023
^{57}Fe(II)-oxalate-hematite	0.80	10.0	1.00	10.0	2.77	−0.08	2.85	0.95	0.28
^{NA}Fe(II)-oxalate-hematite	0.80	10.0	1.00	10.0	4.09	−0.10	4.19	0.02	0.02
AFM-centric experiments									
^{57}Fe(II), aqueous control	—	0.50	—	0.50	−0.02	−0.02	0.00	0.94	0.96
KCl-hematite*	0.04	0.50	—	—	0.00	0.00	0.00	—	—
^{57}Fe(II)-hematite*	0.04	0.50	0.05	—	−0.05	−0.05	0.00	0.94	0.96
Oxalate-hematite*	0.04	0.50	—	0.50	0.01	0.00	0.01	—	0.03
^{57}Fe(II)-oxalate-hematite*	0.04	0.50	0.05	0.50	0.02	−0.01	0.03	0.94	0.40

[a] All reactions were conducted with 12.5 mL, pH 2.3 solutions over 24 hr at 75 °C. [b] Concentrations are reported up to the instruments' analytical precision achieved, *i.e.*, 4% RSD for aqueous Fe concentrations by UV-vis. [c] Concentrations are reported up to the instruments' analytical precision achieved, *i.e.*, 7% RSD for $f_{^{57}Fe}$ by ICP-MS.

composition in solution provides evidence of whether significant iron atom exchange occurs between the solution and solid phase.

For the KCl-hematite reaction, aqueous iron remains below detection limits after reaction (*i.e.*, <0.01 mM); the analytical precision for the UV-vis measurements achieved here is better than 4% relative standard deviation (RSD) (ESI† section 2.1). Thus, the reaction with pH 2.3 KCl does not lead to significant iron release at our conditions, as expected. For the ^{57}Fe(II)-hematite reaction, a low but detectable amount of Fe(II) is removed from solution (*i.e.*, $\Delta Fe(II)_{aq}$ = −0.07 mM), potentially indicative of adsorption onto the particles. A fraction of the Fe(II) removed from solution (*i.e.*, −0.03 mM) may also be due to simple adsorption on the Teflon container walls, based on aqueous control experiments of Fe(II) in solution by itself (*i.e.*, without hematite). Subsequent isotopic imaging by NanoSIMS however provides evidence for ^{57}Fe(II) adsorption to hematite (discussed below). Additionally, there is not a significant change in the iron isotopic composition in solution; *i.e.*, $f_{^{57}Fe\text{-}before}$ and $f_{^{57}Fe\text{-}after}$ (0.95 and 0.98, respectively) are within the instrument's analytical precision (7% RSD for ICP-MS measurements). Fe(III) is not detected in solution. This suggests that iron atom exchange at the hematite surface is likely not extensive under these conditions.

For the oxalate-hematite reaction, net dissolution occurs as the initially iron-free solution accumulates 1.17 mM Fe_{tot}, where Fe(II) and Fe(III) account for 0.44 mM and 0.73 mM, respectively. The iron isotopic composition in solution after reaction reflects NA concentrations ($f_{^{57}Fe\text{-}after}$ = 0.02), in agreement with the notion that the only source of iron in this experiment is the hematite at NA. The presence of both soluble Fe(III) and Fe(II) may reflect several dynamic processes and dissolution stages for mineral dissolution by oxalic acid.[6] That is, ligand-promoted mineral dissolution occurs at the onset of reaction, involving desorption of surface ferric-oxalato complex ions into solution. During the subsequent stage referred to as the induction period, electron transfer between adsorbed oxalate and Fe(III) at the mineral surface occurs (with rates dependent on solution pH, temperature, *etc.*),[5] leading iron dissolution to take the form of Fe(II) rather than Fe(III). When a sufficient amount of soluble ferrous ions has been generated, autocatalytic dissolution becomes operative with oxalate facilitating electron transfer between bridging Fe(II)–Fe(III) surface complexes.

Thus, soluble Fe(III) for the oxalate-hematite reaction here can result from the initial ligand-promoted and/or later autocatalytic dissolution stages, though insight into the contributions from each reaction requires time-dependent analyses (beyond the scope of this paper). The generation of soluble Fe(II) can however be distinctly attributed to reductive-dissolution processes during the induction period, potentially enhanced by the higher temperature and low pH used here.[7,25–28] Photochemical reductive dissolution is insignificant here due to minimal light exposure during reaction in the sealed vessels. Additionally, while oxalate concentrations were not measured in our experiments, the observed generation of soluble Fe(II) implies partial reactive consumption of oxalate, as it would decompose to $CO_{2(g)}$ upon electron transfer.[5] Further, the generation of soluble Fe(II) would enable dissolution to largely proceed as an autocatalytic reaction which, combined with the higher temperature and low pH used here, enhances the rate of dissolution.

In comparison, net dissolution is also observed for the ^{57}Fe(II)-oxalate-hematite reaction but at accelerated rates. That is, more Fe(III) is released into solution ($\Delta Fe(III)_{aq}$ = 2.9 mM) compared to that with oxalate alone. This is because addition of ferrous iron in the initial oxalic acid solution eliminates the time-consuming induction period, enabling autocatalytic dissolution to occur at the onset of reaction.[3,4] Some Fe(II) sorption may also occur ($\Delta Fe(II)_{aq}$ = −0.08), like that for the ^{57}Fe(II)-hematite reaction. The minor deviation

from the initial concentration seemingly indicates equilibrium between soluble and surface adsorbed ferrous ions. Lastly, the isotopic composition of the solution also changes substantially, from the initial $^{57}Fe(II)_{aq}$ to a ^{57}Fe-dilute ($f_{^{57}Fe,before}$ = 0.95 *vs.* $f_{^{57}Fe,after}$ = 0.28) Fe(II)/Fe(III) mixture after reaction. Iron concentration analyses performed on the control $^{NA}Fe(II)$-oxalate-hematite system, without the isotopic labeling present, show similar Fe release behavior ($\Delta Fe(II)_{aq}$ = −0.10 mM, $\Delta Fe(III)_{aq}$ = −4.09 mM; Table 1). Thus, these results confirm enhanced hematite dissolution rates enabled by synergistic interactions between Fe(II) and the chelating ligand.

Microscopic observations of facet-dependent processes

Qualitative observations of morphological and microtopographic evolution. SEM imaging provides general insight into the changes in the morphology and microtopography of the hematite platelets before and after reaction from the bulk batch experiments (Fig. 1), complementing analyses of the aqueous iron fraction. To start, after reaction with KCl (Fig. 1a and e) and $^{57}Fe(II)$ (Fig. 1b and f), significant morphologic changes are not noticeable; *i.e.*, the KCl- and $^{57}Fe(II)$-hematite particles retain well-defined (001) basal and (012) edge surfaces and growth defects such as the intergrowth sites. Spiral growth centers on basal surfaces and emanating bunched step waves parallel to the surface are also still observed. The lack of microtopographic changes over the hematite surfaces is consistent with aqueous analyses, indicating little to no dissolution and/or recrystallization occurs.

For the oxalate-hematite system (Fig. 1c and g), where aqueous analyses indicate net dissolution occurs, the edges and growth defects of particles are similar to that observed for unreacted particles as well as the KCl-hematite standards, although the basal surface is noticeably altered. In contrast to the spiral growth steps typically found on the basal surface, steps on the reacted surface appear straight and aligned with edges of the particles. Pyramidal features on the basal surface are also sparsely observed near the straight-edge steps at times, with minimal to no pitting. While pyramidal features conventionally are not thought to represent dissolution features, they have been observed to form in different materials systems following etching such as silicon[29] and calcite in Pb-rich acidic solutions.[30]

For the $^{57}Fe(II)$-oxalate-hematite reaction, the basal surface is significantly altered after reaction (Fig. 1d and h). It is extensively covered by pyramidal features, qualitatively like those observed in previous studies.[9,10] However, particle

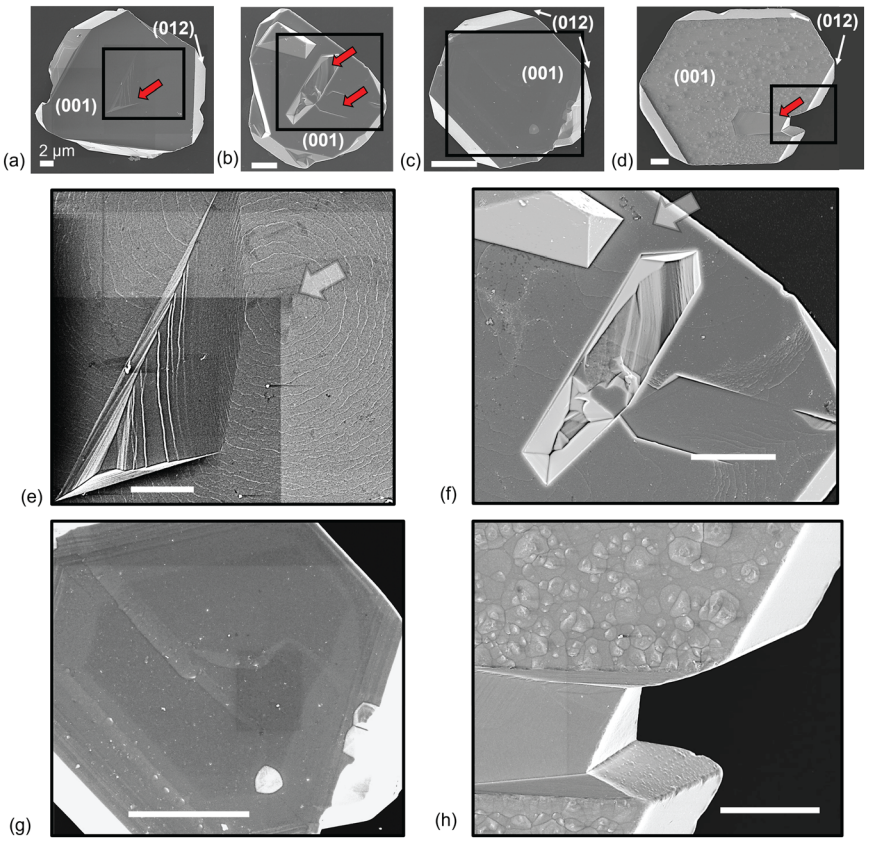

Fig. 1 SEM imaging showing qualitative changes in the particle morphology and microtopographies following reaction with (a and e) KCl, (b and f) $^{57}Fe(II)$, (c and g) oxalate, and (d and h) $^{57}Fe(II)$-oxalate solutions. Higher magnification images of the insets for a–d highlighting the surface topography are shown in e–h, respectively. Red arrows denote intergrowth defects. White transparent arrows denote spiral growth centers. Image contrast/brightness was modified to better resolve surface features. Scale bars represent 2 μm.

edges appear unaltered and the nano-faceted intergrowth defects as they remain smooth and stepped. These observations for the oxalate and Fe(II)-oxalate system show that oxalate preferentially interacts with the basal surface, although the absence or presence of Fe(II) leads to significantly different microtopographies (*i.e.*, smooth and stepped edges on the basal surface *vs.* pyramidal features, respectively). These differences are seemingly linked to the dominant dissolution mechanisms within each respective system where, as described above, rapid autocatalytic dissolution for the ^{57}Fe(II)-oxalate-hematite system leads to extensive formation of pyramidal features on the basal surface compared to that observed for the oxalate-hematite system.

Quantification of microtopographic changes. Correlative AFM analyses on identical platelets before and after reaction were conducted to quantify microscale changes in particles' microtopographies relating to growth and/or dissolution at high resolution, corroborating aqueous analyses. To start, the KCl-hematite* system was analyzed as a control to assess analytical limits for the approach developed here. Qualitatively, the particle microtopography remains unchanged (Fig. 2a) where, for instance, spiral centers observed before reaction are clearly resolved after reaction and the edge faces remain smooth. Aqueous analyses by UV-vis confirm that iron is not released to solution at detectable levels (Table 1). Changes in the basal surface height and lateral dimensions were quantified over the entire particle as well as at select regions. In general, the basal surface height is reproducible within −17 ± 10 nm ($\Delta z_{\text{rxn-avg}}$), based on changes in the average basal height over several particles ($\Delta z_{\text{particle}}$) (Fig. 3a; ESI† Fig. S1a and b). That is, $\Delta z_{\text{particle}}$ measurements show basal surface heights from particle to particle range from −11 ± 6 nm to −25 ± 24 nm (Fig. 3a). The error representing one standard deviation (1SD) shows that the variations in basal height for that specific particle is at the nanometer scale.

Changes in the particle diameters were similarly assessed and found to be generally reproducible, although at lower

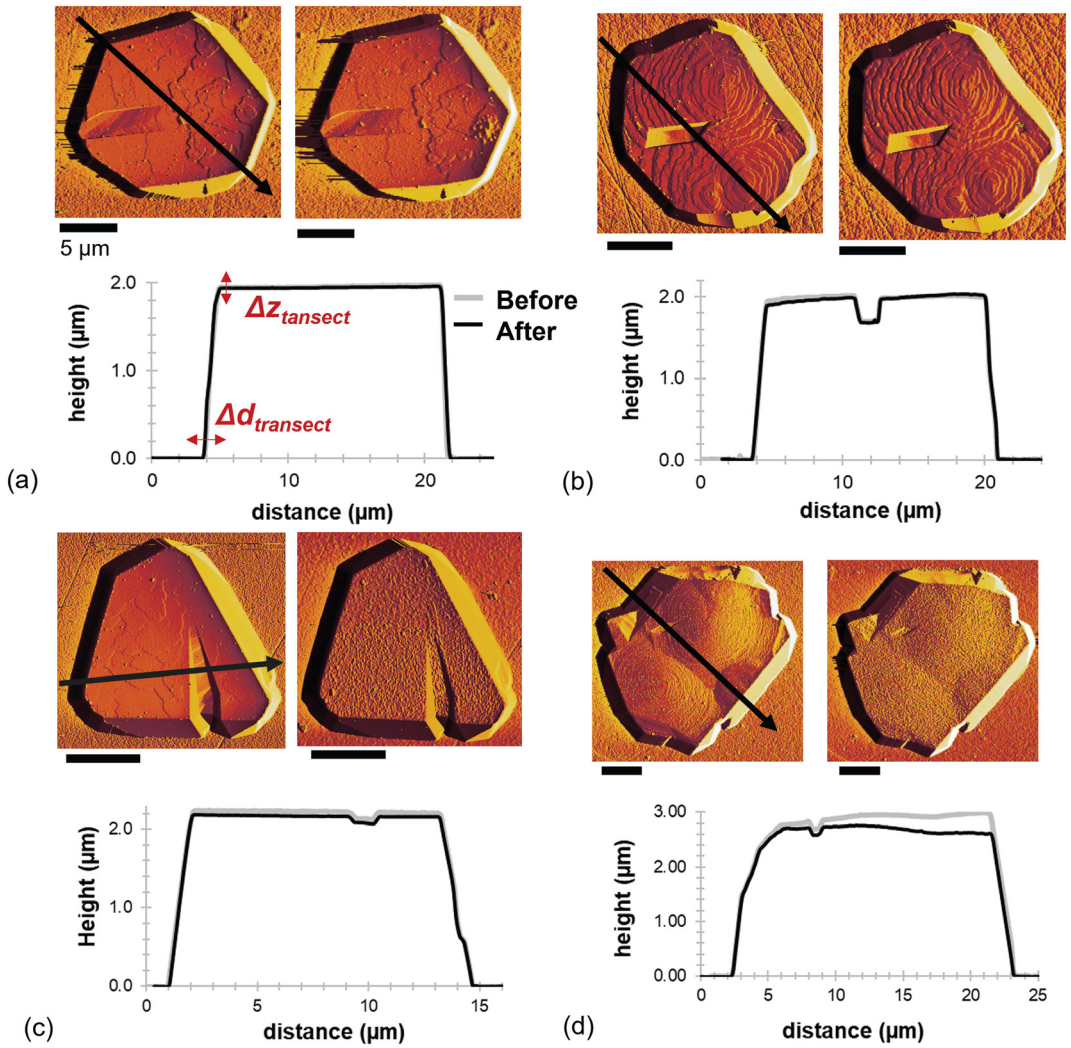

Fig. 2 AFM deflection imaging showing changes in hematite particle microtopography *ex situ*, following reaction with (a) KCl, (b) Fe(II), (c) oxalate, and (d) Fe(II)-oxalate. Transectional analyses from correlative Z-sensor imaging highlights changes in particle heights and diameters across select regions (marked with black arrows). Scale bar in images represents 5 μm.

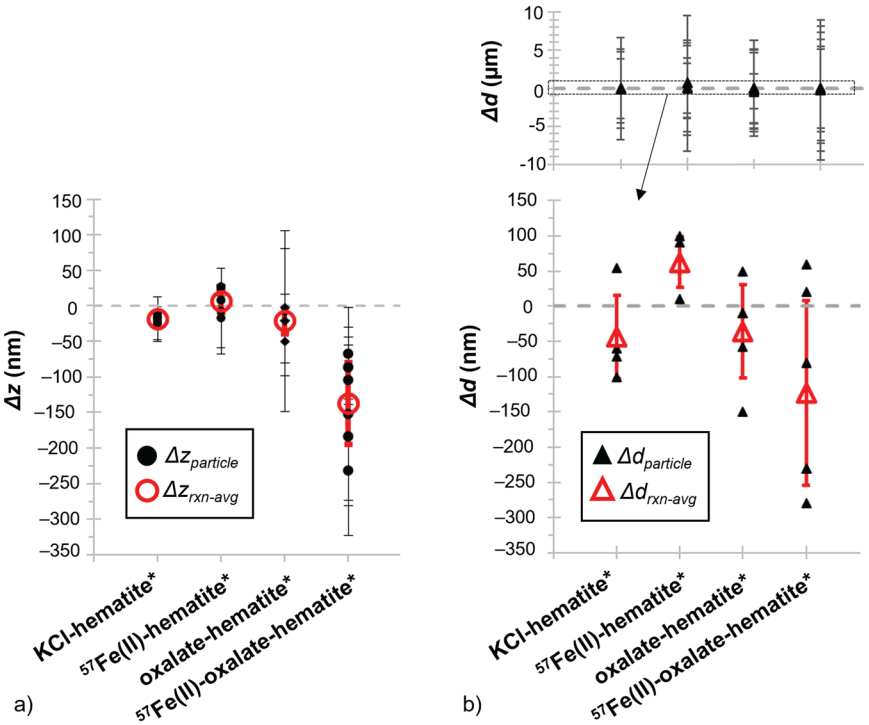

Fig. 3 Changes in (a) basal surface heights and (b) particle diameters measured over several particles, from each reaction. The change in basal height and particle diameter for individual particles is shown for each reaction (black circles for $\Delta z_{particle}$ and black triangles for $\Delta d_{particle}$, respectively). The change in basal height and particle diameter, averaged over all particles, is shown for each reaction (red-open circles for $\Delta z_{rxn\text{-}avg}$ and red-open triangles for $\Delta d_{rxn\text{-}avg}$, respectively). Error bars reflect 1SD. Note the top graph in panel b, shows 1SD values for $\Delta d_{particle}$ are at the micrometer scale.

resolution compared to the basal height measurements. For instance, the diameter across a select region of the KCl-hematite* particle shown in Fig. 2a ($\Delta d_{transect}$) was reproduced within 150 nm after reaction. Moreso, average diameters were generally reproducible within −44 ± 60 nm ($\Delta d_{rxn\text{-}avg}$), based on changes in the average diameter over several particles ($\Delta d_{particle}$) (Fig. 3b; ESI† Fig. S1a and c). The lower resolution for the particle diameter measurements may be due to larger error in tip tracking precision over the steep, tall particle edges. Additionally, the diameter over these non-symmetrical hematite microplatelets can vary at the micrometer scale; for instance, the average diameter of the unreacted KCl-hematite* particle in Fig. 2a is 15.4 ± 4.8 μm. Thus, changes in particle diameters here are considered semi-quantitative.

For the Fe(II)-hematite* reaction, the particle microtopography appears unchanged (Fig. 2b). Based on aqueous analysis by UV-vis, Fe(II) adsorption occurs to some extent, although simple adsorption may also contribute to iron loss from solution (Table 1). Significant changes in the basal heights and/or diameters are not found, as they are within the same order of magnitude error for the control KCl-hematite* reaction ($\Delta z_{rxn\text{-}avg}$ = 7 ± 16 nm, $\Delta d_{rxn\text{-}avg}$ = 63 ± 36 nm; Fig. 3).

For the oxalate-hematite* system, UV-vis and ICP-MS data generally indicate net hematite dissolution occurs for (Fe(II)-) oxalate-hematite* reactions. That is, excess Fe is measured in solution as well following reaction as well as lower $f_{^{57}Fe}$ concentrations (Table 1). However, the extent of dissolution is substantially lower than that in the batch experiments, given the much lower reagent concentrations in these AFM experiments (*i.e.*, 20× lower, see methods section). The basal heights and particle diameters again do not change significantly and are within measurement error (*i.e.*, $\Delta z_{rxn\text{-}avg}$ = −21 ± 19 nm, $\Delta d_{rxn\text{-}avg}$ = −36 ± 66 nm) (Fig. 3). Qualitative observations, however, suggest facet-dependent processes as the basal surface has roughened, consistent with the notion that oxalate preferentially attacks this region (Fig. 2c), while the edges appear unaltered. Straight edge steps like those observed by SEM with the loose powders have not developed, perhaps due to differences in dissolution inherent in the design of the AFM experiments.

For the ^{57}Fe(II)-oxalate-hematite* system, imaging and topographic profiles indicate minimal alteration to the edge facets while pyramid formation occurs on the basal surface, consistent with loose powder experiments (Fig. 2d and 4). More so, the basal surface heights decrease significantly relative to the other reactions ($\Delta z_{rxn\text{-}avg}$ = −137 ± 57 nm), outside measurement error (Fig. 3a). This is consistent with preferential dissolution of (001). Measured changes in the particle diameter suggest these may also decrease relative to the other reactions ($\Delta z_{rxn\text{-}avg}$ = −123 ± 131 nm), though this is difficult to conclude due to the stated higher error when measuring particle diameters.

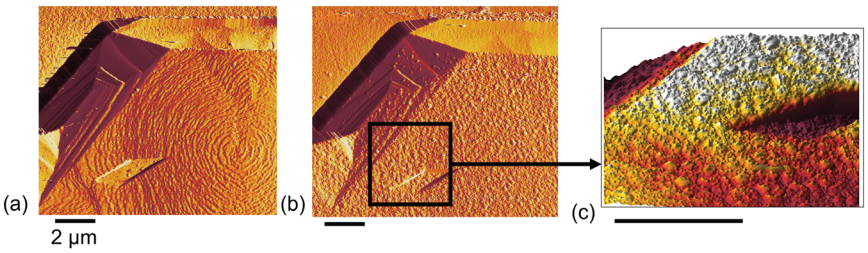

Fig. 4 Higher magnification AFM deflection image from the ^{57}Fe(II)-oxalate-hematite particle from Fig. 3d, showing the evolution of the basal and edge surfaces as well as an intergrowth feature (a) before and (b) after reaction. (c) A higher magnification and rotated 3D image from the region in panel b, highlighting the pyramidal microtopography. Scale bar is 2 μm.

Furthermore, measurements show dissolution across the basal surface of a single particle can be anisotropic. For instance, if looking at the height profile for the transect across the particle before and after reaction (Fig. 2d), one end of the basal surface (*i.e.*, at 7 μm) has dissolved by ~100 nm (*i.e.*, height changes from ~2.7 μm to ~2.6 μm) while at the opposite end the basal surface has dissolved by ~400 nm. Additionally, dissolution can be heterogeneous at intergrowth defects compared to the basal surface, as observed with the loose powder experiments (Fig. 4). For instance, the steps of an intergrowth defect towards the basal surface can exhibit pyramidal features while the steps moving away exhibit no alteration. Thus, it seems site-specific differences exist leading to local variations in the dissolution kinetics and particle morphologic evolution, a finding that lies beyond the scope of the present paper.

Probing ^{57}Fe deposition-recrystallization by isotopic imaging techniques. Aqueous chemical and microscopic analyses show net dissolution for the oxalate and Fe(II)-oxalate systems while the KCl- and Fe(II)-hematite particles are not discernably altered. The collective microscopic observations by AFM and SEM are consistent with the indications from the solution analyses that the Fe(II)-oxalate-hematite system leads to the most facile dissolution, coupled to the most dramatic changes in the surface microtopography, primarily of the basal surface. While net dissolution of hematite prevails in the presence of Fe(II)-oxalate, previous studies present the potential for simultaneous redeposition/recrystallization to also occur.[9,10] That is, Yanina and Rosso[9] observed that the pyramidal morphology on the basal surface does not form unless basal surfaces are electrically connected to vicinal edge surfaces (*i.e.*, bicrystal experiments under more concentrated conditions). In turn, recrystallization leading to coupled edge and basal surface morphologic evolution was inferred. Iron deposition on hematite microplatelets during reaction with ^{57}Fe(II)-oxalate (again in more concentrated solutions) was also inferred by Mossbauer spectroscopy.[10] Thus, while the pyramidal morphology is qualitatively similar to that observed in previous work, it is not clear if the underlying processes are identical those in this study.

Here, we aimed to directly examine the prospect that surface microtopographic evolution entails a combination of both depositional and detachment processes (*i.e.*, recrystallization), by focusing on resolving ^{57}Fe incorporation in the basal surfaces of single-particles using mass-sensitive imaging methods. Isotopic imaging and analysis by NanoSIMS were conducted on ^{57}Fe(II)-reacted hematite particles (^{57}Fe(II)-hematite and ^{57}Fe(II)-oxalate-hematite) and a control (^{NA}Fe(II)-oxalate-hematite) from the bulk batch experiments, to probe whether ^{57}Fe from solution associates with particular regions/surfaces. Here, $^{54}Fe^{16}O^-$ and $^{57}Fe^{16}O^-$ secondary ions were measured using a Cs^+ primary ion beam.

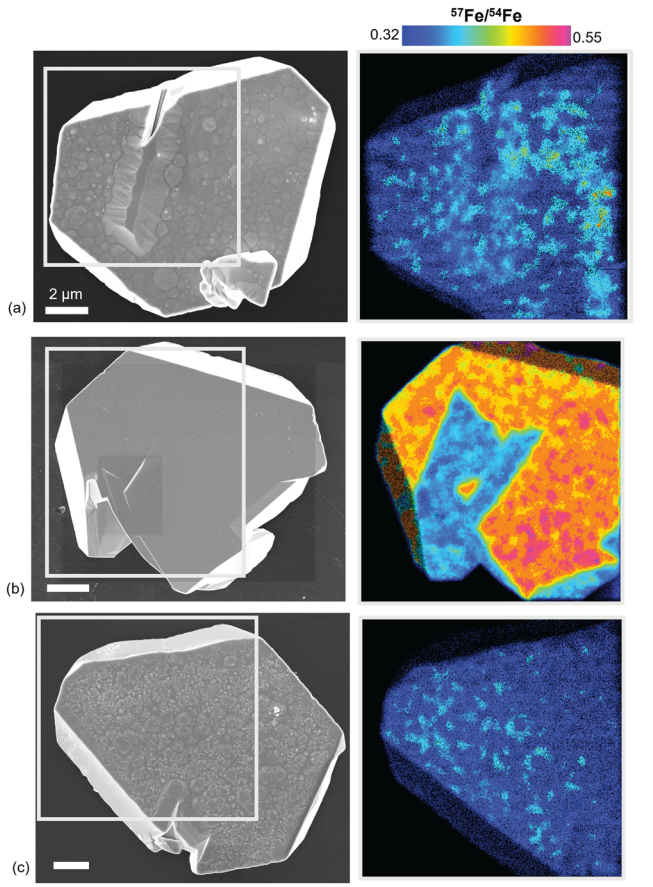

Fig. 5 Morphological characteristics shown by SEM and correlative NanoSIMS isotopic mapping on the (a) control ^{NA}Fe(II)-oxalate-hematite, (b) ^{57}Fe(II)-hematite, (c) ^{57}Fe(II)-oxalate-hematite samples.

The iron isotopic composition was determined as $^{57}Fe^{16}O^-/^{54}Fe^{16}O^-$, hereafter referred to as just "$^{57}Fe/^{54}Fe$".

Fe isotopic measurements on the ^{NA}Fe(II)-oxalate-hematite control establish NA isotopic concentrations for the NanoSIMS analyses. That is, the average $^{57}Fe/^{54}Fe$ measured across two particles was 0.36 ± 0.01 (error represents one standard deviation) (Fig. 5a), in good agreement with that expected at NA (*i.e.*, $^{57}Fe/^{54}Fe$ = 0.36). Further, the control specimen's microtopography is like that observed for the ^{57}Fe(II)-oxalate-hematite system, accounting for effects of surface topography on visualization/quantification of the iron isotopic composition. That is, surface topography may lead to slight variations in isotopic measurements (*i.e.*, per mille level) where, for instance, it was previously shown that high precision $\delta^{18}O$ measurements for magnetite[31] and $\delta^{56}Fe$ measurements for hematite[32] by SIMS was affected by crystal orientation. The surface topography here however does not lead to considerable deviations in $^{57}Fe/^{54}Fe$ composition of the control, as isotopic maps show the $^{57}Fe/^{54}Fe$ composition across the particle is uniform.

Analyses on ^{57}Fe(II)-hematite particles serve as a reference system where the surface is isotopically enriched, *i.e.*, *via* adsorption of soluble iron, and thus exhibits more significant isotopic contrast. For the particle in Fig. 5b, $^{57}Fe/^{54}Fe$ measurements across various surfaces and sites over a single particle can range from 0.37–0.51. Higher $^{57}Fe/^{54}Fe$ ratios are outside the uncertainty for NA and thus effectively indicate the presence of ^{57}Fe-enriched regions. More so, isotopic maps show distinct facet- and site-selective trends for Fe(II) adsorption at pH 2; *i.e.*, (001) and (012) surfaces are ^{57}Fe-enriched (0.51 ± 0.01) while intergrowth defects are not enriched and within error of NA (0.35 ± 0.01). In a previous study, Fe(II) adsorption onto hematite at pH 7.5 was found to preferentially bind to (001) relative to the edges while intergrowth defects were unreactive.[18] Similar facet-specific uptake behavior is observed here, even with much more acidic conditions.

For the ^{57}Fe(II)-oxalate-hematite sample, isotopic enrichment at the basal surface is not observed (Fig. 5c). That is, $^{57}Fe/^{54}Fe$ measured across the particle surfaces are similar to that of the control sample (0.35 ± 0.01) and within NA. $^{57}Fe/^{54}Fe$ maps show that the isotopic composition across the particle is also effectively uniform. Trends in facet- and/or site-selective adsorption of Fe(II) are not observed, and enrichment of the pyramids on the basal surface is not obvious. The observed behavior is consistent with dissolution prevailing on basal surfaces.

Considering the possibility that the pyramidal morphology could result from coupled dissolution and redeposition during recrystallization, we also probed potential ^{57}Fe

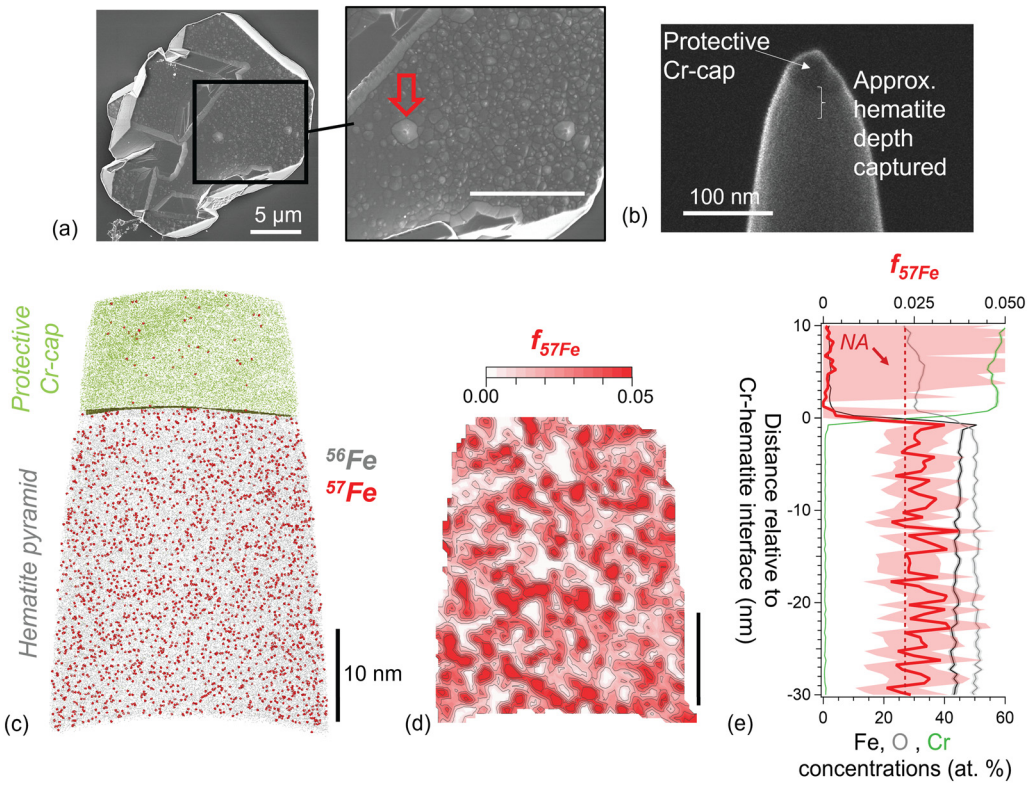

Fig. 6 Distribution of ^{57}Fe within a pyramidal feature from a ^{57}Fe(II)-oxalate-hematite particle, probed by APT. (a and b) SEM imaging showing the pyramidal feature on a reacted particle chosen for analysis and (b) the corresponding APT specimen. (c) APT atomic reconstruction showing the distribution of ^{57}Fe (red atoms) relative to ^{56}Fe (gray atoms) and protective Cr-coating (green). (d) 2D concentration plot of $f_{^{57}Fe}$ showing the ^{57}Fe distribution in the hematite volume in a 5 nm cross-section. (e) Proximity histogram concentration profile relative to the Cr-hematite interface (using an isosurface of 50 atomic% Cr), showing $f_{^{57}Fe}$ in hematite at depth. Dashed red line represents $f_{^{57}Fe}$ at NA.

incorporation at depth within pyramidal features of ^{57}Fe(II)-oxalate-hematite particles by APT. Larger pyramids on the basal surface particle (≥~300 nm) were prepared into APT specimens (protected by a Cr-coating, see ESI† Fig. S2 and section 2.4 for preparation details), to analyze the nanoscale isotopic distribution at depth and/or spatially (Fig. 6a and b). In a representative APT chemical reconstruction for a pyramidal feature, atomic maps and 2D concentration plots for $f_{^{57}Fe}$ show the distribution of ^{57}Fe is effectively uniform within the pyramidal feature over an ~40 nm depth (Fig. 6c and d). ^{57}Fe-enriched regions/features (*e.g.*, clusters) are not readily identified. Statistical analyses and random comparator techniques (described in the ESI† section 2.4 and Taylor, *et al.*[19]) further confirm observations that ^{57}Fe is randomly and uniformly distributed within the hematite (*i.e.*, with a Pearson coefficient μ = 0.11). A concentration profile (described by the proximity histogram approach)[33] also shows that $f_{^{57}Fe}$ averaged over an ~30 nm depth within hematite is at NA (Fig. 6e). Thus, ^{57}Fe is uniformly distributed over the hematite volume analyzed here and there is no lasting evidence of ^{57}Fe(II) from solution adsorbed on particle surfaces or incorporated at depth.

Discussion

The collective findings demonstrate dissolution of hematite prevails in the presence of Fe(II)-oxalate at our reaction conditions, in conceptual agreement with the autocatalytic model put forward in early batch experiments based on solution analyses.[3,4,7] The morphologic evolution of the hematite platelets are similar to those observed in Rosso, *et al.*,[10] although ^{57}Fe deposition detected in that study by using Mossbauer spectroscopy on bulk powder samples could not be verified here through mass-sensitive imaging at the single particle level. While the reaction conditions are not identical, they produce qualitatively similar microtopographic evolution of the microplatelets. Further, through combined characterizations of the solution and solid phases, the present study establishes that iron re-adsorption and deposition is unlikely to be involved in the development of the pyramidal morphology. Rather, this feature results from net dissolution of the hematite basal surface, as shown by excess iron measured in solution following reaction and decreases in the basal height of reacted particles quantified by *ex situ* AFM. In the absence of oxalate, a minor amount of growth/recrystallization is detected, particularly on (001) basal surfaces, consistent with our prior related work using NanoSIMS[18] as well as conceptually related to studies using other single-crystal surface characterization techniques such as X-ray reflectivity.[34]

It is possible the lack of evidence for ^{57}Fe deposition in the ^{57}Fe(II)-oxalate-hematite system here may be limited by small sample sizes (*e.g.*, single particles *vs.* averaged over thousands of particles) and small sampling regions (*e.g.*, micrometer to nanometer scale) inherent to these isotopic imaging techniques. For instance, these analyses cannot address the potential for ^{57}Fe to be buried at greater depths and/or localized outside areas probed. Additionally, if ^{57}Fe deposition occurs concurrent with hematite dissolution and release of ^{56}Fe a mixed isotopic phase may form, as is the case for homogeneous recrystallization,[13,14,35] where the isotopic contrast would be muted and potentially near detection limits for the techniques applied here. However, given the several approaches applied to follow the iron provenance between the solution and solid phases over a range of scales and that overall these measurements are internally consistent, collectively these results clearly demonstrate net dissolution prevails at the reaction conditions used in this study.

Systematic analyses on the interactions between hematite and Fe(II), oxalate, and Fe(II)-oxalate highlight the anisotropic properties and reactivity of hematite. The microtopographic evolution relative to the chemical conditions also indicates that markedly diverse dissolution mechanisms are at play. For instance, on the basal surface there is a stark contrast between the pyramidal morphology that develops in Fe(II)-oxalate *versus* the smooth and stepped surfaces resulting from oxalate alone. Whereas in Fe(II) alone, the particle microtopography was effectively unaltered, despite clear evidence for highly facet-selective ^{57}Fe(II) adsorption on both (001) and (012) surfaces (*i.e.*, ^{57}Fe/^{54}Fe = 0.51 ± 0.01) while intergrowth defect features show no enrichment within error relative to NA (0.35 ± 0.01).

Facet- and pH-dependent relationships for Fe(II) adsorption begin to emerge, particularly when compared to our recent studies on Fe(II) adsorption onto hematite microplatelets at pH 7, where facet-selective trends arose: (001) ≫ (012) ≈ (110) ≫ intergrowth defects.[18] At pH 2, the ^{57}Fe-enrichment on (001) and (012) are generally comparable, indicating pH-dependent changes in the facet-selectivity for Fe(II). Furthermore, consistent with prior related work, it appears that oxalate is particularly well-suited to form complexes on the (001) surface. That is, during the reductive dissolution of hematite particles by ascorbic acid, rapid dissolution of (001) was associated with the formation of bidentate mononuclear Fe-ascorbate complexes while slow dissolution of (012) surfaces was due to the formation of monodentate mononuclear complexes.[36] Similarly, oxalate has been shown to form bidentate complexes on loose hematite powders at pH 5, where two oxygens bind to a single surficial Fe atom,[8] which are prevalent on the (001) surface.[37] Thus, these structural details help explain the observed preferential binding of oxalate to (001), yielding highly facet-dependent dissolution.

The connections between macroscopic dissolution rates and surface-specific structures put forth here are likely broadly applicable to understanding iron oxide reactivity. For instance, we speculate that the enhanced dissolution of loose hematite powders by iron chelating ligands forming bidentate mononuclear surface complexes (*i.e.*, oxalate, malonate, and glutarate) at pH 5, compared to those that formed monodentate surface structures (succinate and adipate),[8] could again be related to the specific structural

details at basal *vs.* edge surfaces. Along these lines, it would be interesting to extend this approach to observe the effects of interchanging chelating ligands on crystal growth, dissolution, and/or recrystallization. For instance, we anticipate that the presence of chelating ligands with bidentate *vs.* monodentate binding complexes could cause mineral facets to dissolve and/or growth at different rates, in turn leading to unique morphological evolution. Effects from pH, temperature, chelating ligand and/or $Fe(II)_{aq}$ concentrations, *etc.*, may afford further opportunities to precisely regulate mineral interfacial reactivities. The insights from these studies could in turn be applied towards understanding crystallization processes in more complex natural environments (*e.g.*, in the presence of various organic ligands) as well as offer new potential remediation strategies based on facet-specific engineering and reactivity of materials.[16]

Conclusions

The autocatalytic interaction between Fe(II)-oxalate solutions and hematite is important because of its relevance to reductive/ligand-assisted metal oxide dissolution mechanisms in environmental systems and in industry. Comprehensive knowledge of mass transfer processes that govern the morphologic evolution of faceted hematite platelets has remained limited to examination of either solution analyses or solids characterization, but not both simultaneously, until the present study. Here a multimodal approach based largely on iron isotopic labelling and mass-sensitive imaging to monitor iron mass transport between the aqueous and solid phase as well as across solid interfaces shows that the system evolution is largely consistent with net dissolution. Systematic study of the effects of the different components present (*i.e.*, Fe(II), oxalate, Fe(II)-oxalate), along with distinct facet expression, demonstrate their roles during reaction as well as the diverse dissolution/growth mechanisms that obtain. Facet-selective adsorption of Fe(II) on hematite and growth occurs in the presence of Fe(II) alone, and is pH-dependent. Dissolution occurs in the presence of oxalate and Fe(II)-oxalate, and is shown to be facet-dependent. Particle dissolution is heavily impacted by the presence of Fe(II) together with oxalate, where in the absence of Fe(II) dissolution occurs *via* step retreat while in the presence of Fe(II) etching along [001] is preferred.

The ability to monitor mass transport and the flux of iron atoms within the solution and solid phases can provide considerable insight into facet-selective dissolution, readsorption, or recrystallization reaction mechanisms. The multimodal approach described here can be applied to probe complex crystal dissolution-readsorption processes across a broad range of materials. For the present system, further work exploring condition-specific behavior would be valuable. For example, it would be of interest to tune conditions to determine if regimes exist where recrystallization *via* growth and dissolution occurs in tandem. In addition to the effects from pH, temperature, chelating ligand and/or $Fe(II)_{aq}$ concentrations, *etc.*, we postulate that the balance between these two competing processes could be achieved by varying the ratio of Fe(II):oxalate. For instance, under the experimental conditions used re-adsorption of Fe tends to be inhibited by oxalate. However, excess Fe(II) not complexed by oxalic acid could lead to uptake by hematite. If such conditions could be found, it would be particularly interesting to examine with isotopic imaging techniques the distribution of iron isotopes spatially with respect to facets and surface features, as well as with depth to uncover burial mechanisms.

More broadly, this study clearly reveals substantial anisotropy in the interfacial reactivity of iron oxide crystallites, important to understanding their behavior in a variety of contexts such as their use for contaminant remediation,[16,38,39] light-induced water splitting and photocatalysis, or as a model for mineral-associated organic matter.[8,36] The approaches developed here can be applied to probe and understand a wide variety of autocatalytic processes on metal oxide surfaces. Continued investigation on the synergistic interactions between Fe(II) and chelating ligands, like dicarboxylic acids, with iron oxide crystallites exposing various facets in particular can offer unique opportunities for tuning interfacial reactivities as well as regulating mineral dissolution, growth, and recrystallization. Given the wide-ranging applications for hematite in natural and engineered environments, insight into these fundamental interfacial properties would of broad significance, from predicting the biogeochemical cycling of iron to developing tailored hematite nanocrystals as selective contaminant remediation substrates.

Data availability

The data supporting this article have been included in the main text as well as in the ESI.†

Conflicts of interest

There are no conflicts of interest to declare.

Acknowledgements

This material is based upon work supported by the U.S. Department of Energy (DOE), Office of Science, Basic Energy Sciences (BES), Chemical Sciences, Geosciences, and Biosciences Division through its Geosciences Program at Pacific Northwest National Laboratory (PNNL) (FWP 56674). A portion of the work was performed in the Environmental and Molecular Sciences Laboratory (EMSL), a national scientific user facility at PNNL sponsored by the DOE's Office of Biological and Environmental Research, under user proposals **https://doi.org/10.46936/lser.proj.2020.51382/60000186** and **https://doi.org/10.46936/lser.proj.2021.51922/60000373**. PNNL is a multi-program national laboratory operated by Battelle Memorial Institute under contract number DE-AC05-76RL01830 for the DOE.

References

1 A. G. B. Williams and M. M. Scherer, Spectroscopic evidence for Fe(II)–Fe(III) electron transfer at the iron oxide–water interface, *Environ. Sci. Technol.*, 2004, **38**, 4782–4790.
2 B. Zinder, G. Furrer and W. Stumm, The coordination chemistry of weathering: II. Dissolution of Fe(III) oxides, *Geochim. Cosmochim. Acta*, 1986, **50**, 1861–1869.
3 D. Suter, C. Siffert, B. Sulzberger and W. Stumm, Catalytic dissolution of iron(III) (hydr)oxides by oxalic-acid in the presence of Fe(II), *Naturwissenschaften*, 1988, **75**, 571–573.
4 S. Banwart, S. Davies and W. Stumm, The role of oxalate in accelerating the reductive dissolution of hematite (α-Fe_2O_3) by ascorbate, *Colloids Surf.*, 1989, **39**, 303–309.
5 M. Taxiarchou, D. Panias, I. Douni, I. Paspaliaris and A. Kontopoulos, Dissolution of hematite in acidic oxalate solutions, *Hydrometallurgy*, 1997, **44**, 287–299.
6 D. Panias, M. Taxiarchou, I. Douni, I. Paspaliaris and A. Kontopoulos, Dissolution of hematite in acidic oxalate solutions: The effect of ferrous ions addition, *Hydrometallurgy*, 1996, **43**, 219–230.
7 D. Panias, M. Taxiarchou, I. Paspaliaris and A. Kontopoulos, Mechanisms of dissolution of iron oxides in aqueous oxalic acid solutions, *Hydrometallurgy*, 1996, **42**, 257–265.
8 O. W. Duckworth and S. T. Martin, Surface complexation and dissolution of hematite by C-1-C-6 dicarboxylic acids at pH=5.0, *Geochim. Cosmochim. Acta*, 2001, **65**, 4289–4301.
9 S. V. Yanina and K. M. Rosso, Linked reactivity at mineral-water interfaces through bulk crystal conduction, *Science*, 2008, **320**, 218–222.
10 K. M. Rosso, S. V. Yanina, C. A. Gorski, P. Larese-Casanova and M. M. Scherer, Connecting observations of hematite (a-Fe_2O_3) growth catalyzed by Fe(II), *Environ. Sci. Technol.*, 2010, **44**, 61–67.
11 R. T. Shuey and D. F. Pridmore, Electronic properties of ore minerals and their geophysical implications, *Geophysics*, 1975, **40**, 155–156.
12 A. H. Morrish, *Canted antiferromagnetism: Hematite*, 1994.
13 C. A. Gorski and M. S. Fantle, Stable mineral recrystallization in low temperature aqueous systems: A critical review, *Geochim. Cosmochim. Acta*, 2017, **198**, 439–465.
14 P. Joshi, M. S. Fantle, P. Larese-Casanova and C. A. Gorski, Susceptibility of goethite to Fe^{2+}-catalyzed recrystallization over time, *Environ. Sci. Technol.*, 2017, **51**, 11681–11691.
15 J. Huang, A. Jones, T. D. Waite, Y. Chen, X. Huang, K. M. Rosso, A. Kappler, M. Mansor, P. G. Tratnyek and H. Zhang, Fe(II) redox chemistry in the environment, *Chem. Rev.*, 2021, **121**, 8161–8233.
16 X. P. Huang, X. J. Hou, X. Zhang, K. M. Rosso and L. Z. Zhang, Facet-dependent contaminant removal properties of hematite nanocrystals and their environmental implications, *Environ. Sci.:Nano*, 2018, **5**, 1790–1806.
17 P. Larese-Casanova and M. M. Scherer, Fe(II) sorption on hematite: New insights based on spectroscopic measurements, *Environ. Sci. Technol.*, 2007, **41**, 471–477.
18 S. D. Taylor, L. Kovarik, J. B. Cliff and K. M. Rosso, Facet-selective adsorption of Fe(II) on hematite visualized by nanoscale secondary ion mass spectrometry, *Environ. Sci.: Nano*, 2019, **6**, 2429–2440.
19 S. D. Taylor, J. Liu, B. W. Arey, D. K. Schreiber, D. E. Perea and K. M. Rosso, Resolving iron(II) sorption and oxidative growth on hematite (001) using atom probe tomography, *J. Phys. Chem. C*, 2018, **122**, 3903–3914.
20 S. D. Taylor, J. Liu, X. Zhang, B. W. Arey, L. Kovarik, D. K. Schreiber, D. E. Perea and K. M. Rosso, Visualizing the iron atom exchange front in the Fe(II)-catalyzed recrystallization of goethite by atom probe tomography, *Proc. Natl. Acad. Sci. U. S. A.*, 2019, **116**, 2866.
21 R. S. Sapieszko and E. Matijevic, Preparation of well-defined colloidal particles by thermal-decomposition of metal-chelates I. Iron oxides, *J. Colloid Interface Sci.*, 1980, **74**, 405–422.
22 L. Taijing and I. Sunagawa, Origin of undulated growth steps on hematite crystals from Sasazawa, Japan, *Mineral. J.*, 1987, **13**, 409–423.
23 C. Siffert and B. Sulzberger, Light-induced dissolution of hematite in the presence of oxalate. A case study, *Langmuir*, 1991, **7**, 1627–1634.
24 J. Riemer, H. H. Hoepken, H. Czerwinska, S. R. Robinson and R. Dringen, Colorimetric ferrozine-based assay for the quantitation of iron in cultured cells, *Anal. Biochem.*, 2004, **331**, 370–375.
25 R. Torres, M. A. Blesa and E. Matijevic, Interactions of metal hydrous oxides with chelating-agents .9. Reductive dissolution of hematite and magnetite by aminocarboxylic acids, *J. Colloid Interface Sci.*, 1990, **134**, 475–485.
26 R. Torres, M. A. Blesa and E. Matijevic, Interactions of metal hydrous oxides with chelating-agents .8. Dissolution of hematite, *J. Colloid Interface Sci.*, 1989, **131**, 567–579.
27 H.-C. Chang and E. Matijević, Interactions of metal hydrous oxides with chelating agents: IV. Dissolution of hematite, *J. Colloid Interface Sci.*, 1983, **92**, 479–488.
28 G. Zhan, Y. Fang, M. Zhang, S. Cao, T. Xu, C. Ling, H. Gu, X. Liu and L. Zhang, Oxalate promoted iron dissolution of hematite via proton coupled electron transfer, *Environ. Sci.: Nano*, 2022, **9**, 1770–1779.
29 W. Chen, Y. Liu, L. Yang, J. Wu, Q. Chen, Y. Zhao, Y. Wang and X. Du, Difference in anisotropic etching characteristics of alkaline and copper based acid solutions for single-crystalline Si, *Sci. Rep.*, 2018, **8**, 3408.
30 K. Yuan, V. De Andrade, Z. E. Feng, N. C. Sturchio, S. S. Lee and P. Fenter, Pb^{2+}-calcite interactions under far-from-equilibrium conditions: Formation of micropyramids and pseudomorphic growth of cerussite, *J. Phys. Chem. C*, 2018, **122**, 2238–2247.
31 J. M. Huberty, N. T. Kita, R. Kozdon, P. R. Heck, J. H. Fournelle, M. J. Spicuzza, H. F. Xu and J. W. Valley, Crystal orientation effects in $\delta^{18}O$ for magnetite and hematite by SIMS, *Chem. Geol.*, 2010, **276**, 269–283.
32 N. T. Kita, J. M. Huberty, R. Kozdon, B. L. Beard and J. W. Valley, High-precision SIMS oxygen, sulfur and iron stable

isotope analyses of geological materials: Accuracy, surface topography and crystal orientation, *Surf. Interface Anal.*, 2011, **43**, 427–431.

33 O. C. Hellman, J. A. Vandenbroucke, J. Rusing, D. Isheim and D. N. Seidman, Analysis of three-dimensional atom-probe data by the proximity histogram, *Microsc. Microanal.*, 2000, **6**, 437–444.

34 J. G. Catalano, P. Fenter, C. Park, Z. Zhang and K. M. Rosso, Structure and oxidation state of hematite surfaces reacted with aqueous Fe(II) at acidic and neutral pH, *Geochim. Cosmochim. Acta*, 2010, **74**, 1498–1512.

35 P. Zarzycki and K. M. Rosso, Energetics and the role of defects in Fe(II)-catalyzed goethite recrystallization from molecular simulations, *ACS Earth Space Chem.*, 2019, **3**, 262–272.

36 X. Huang, X. Hou, F. Song, J. Zhao and L. Zhang, Ascorbate induced facet dependent reductive dissolution of hematite nanocrystals, *J. Phys. Chem. C*, 2017, **121**, 1113–1121.

37 T. P. Trainor, A. M. Chaka, P. J. Eng, M. Newville, G. A. Waychunas, J. G. Catalano and G. E. Brown, Structure and reactivity of the hydrated hematite (0001) surface, *Surf. Sci.*, 2004, **573**, 204–224.

38 S. D. Taylor, M. C. Marcano and U. Becker, A first principles investigation of electron transfer between Fe(II) and U(VI) on insulating Al- vs. semiconducting Fe-oxide surfaces via the proximity effect, *Geochim. Cosmochim. Acta*, 2017, **197**, 305–322.

39 S. D. Taylor, U. Becker and K. M. Rosso, Electron transfer pathways facilitating U(VI) reduction by Fe(II) on Al- vs Fe-oxides, *J. Phys. Chem. C*, 2017, **121**, 19887–19903.